

Research Article

The Simulation on Temperature and Thermal Stress of Leakage Current Particulate Matter Sensor on Diesel Engine

Dong Tang , **Li Wang** , **Yang Liu** , **Ning Liu** , and **Yuzhe Wu** 

Department of Automotive and Traffic Engineering, Jiangsu University, Zhenjiang 212013, China

Correspondence should be addressed to Li Wang; 18352866647@163.com

Received 8 May 2019; Revised 8 August 2019; Accepted 27 August 2019; Published 13 October 2019

Academic Editor: Bruno C. Janegitz

Copyright © 2019 Dong Tang et al. This is an open access article distributed under the Creative Commons Attribution License, which permits unrestricted use, distribution, and reproduction in any medium, provided the original work is properly cited.

Based on the working environment and control strategy of the leakage current particulate sensor on the diesel engine, the ANSYS finite element simulation is applied to prove the reliability of the sensor in the response phase. It shows that the full load conditions of the diesel engine harsh the exhaust environment, which leads to higher thermal stress in the sensor. The temperature of the front end of the sensor base is up to 227°C, and the highest thermal stress appearing in the sensor is 88 MPa. Both of them are lower than the upper limit request, which guarantees the working reliability of the sensor in long period. The effect of outside environment on the highest temperature of the sensor base is also investigated, and it shows that the lower temperature and the higher convective heat transfer coefficient would be in favor of the reliable work of the sensor. In addition, it shows that the cold start time of the sensor is reducing exponentially with the increasing heating power, and the optimum heating power is 60 W taking the linearly increasing thermal stress into consideration.

1. Introduction

It is an undeniable fact that the diesel engine is better than any other thermal engines when it comes to the advantage of energy conservation and little CO₂ emission [1]. However, it is inevitable that the particulate matter (PM) emission and soluble friction (SOF) emission from the diesel engine may influence the health of people. Hence, diesel particulate filter is widely used to reduce the PM emission in European and American [2].

According to the OBD emission regulations issued in California (USA) in 2013, PM emission is required to be lower than 10.8 mg/km [3]. The OBD thresholds for light cars and heavy cars in Europe are 12 mg/km and 25 mg/km, respectively [4]. As for it, the pressure difference sensor with poor sensitivity cannot meet the OBD standard of Europe and America. PM sensor can satisfy the requirement of the abovementioned OBD standard, because it can acquire the mass concentration of PM in exhausted gas, which can directly infer and adjust the working status of DPF. Therefore, the demand for the new high-precision PM sensors is becoming more and more urgent [5–7]. Recently, PM sen-

sors based on different working principles have appeared. Based on the multilayer ceramic technology, the resistive and capacitive PM sensor developed jointly by BOSCH (Germany) and NTK (Japan) converts resistance and capacitance values into PM concentration [6, 8]. Picasso in Finland proposed the charging current difference PM sensor, where corona charger is put in the sensor Faraday cup. The current difference before and after charging the Faraday Cup is acquired by the electrometer in the sensor, which can imply the PM concentration [9, 10].

The prototype mechanism of the leakage current PM sensor is originally proposed by Steppan et al. of Emisense Technologies, LLC. to detect the PM concentration [11]. Figure 1 shows the diagram of PM sensor of Emisense Technologies, LLC [12, 13], and the head of the sensor is vertically installed in the exhaust pipe downstream of the DPF. The concentration test zone based on the principle of capacitance locates between the central electrode and the internal baffle. The working principle of PM sensor is as follows. Pressure difference contributes the exhausted gas to flow into the concentration test zone. Then, PM in the exhaust gas is ionized or polarized into conductors under the high voltage, and

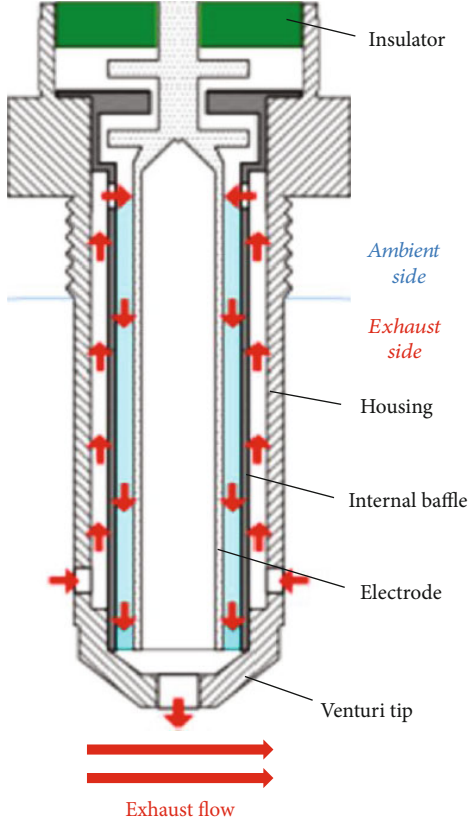


FIGURE 1: Diagram of the sensor.

leakage current generates between the electrode and the internal baffle [14]. The leakage current varies with the change of the concentration of the PM in the concentration test zone. Therefore, the concentration of PM can be implied by measuring the leakage current. The microcurrent of nA level collected by the sensor would be converted to the voltage signal positive to the current by the sensor control unit (SCU), and the voltage signal ranges from 0 to 5 V [15, 16]. Compared with other PM sensors, leakage current PM sensor possesses the following advantages: real-time monitor of PM concentration, long working period without frequent regeneration, and low cost.

To optimize the structure of the sensor, the ANSYS software is employed to simulate the temperature and stress distribution of the sensor by changing the environment parameters and structure parameters of the sensor. And the optimum heating power is investigated under the circumstance of the engine working at idling speed.

2. Simulation

2.1. Numerical Method. In this paper, the finite element method is used to simulate the temperature and thermal stress distribution by ANSYS software, where the structure (solving domain) is divided into finite units, all of which gathered are approximately equivalent to the original structure. Then, the sum of the simulated results of all units is used as the simulated results of the whole solving domain. In 1963, Besseling et al. demonstrated that the finite element method

is another form of the Ritz method based on the variational principle [17, 18].

The temperature change of the object will cause the thermal deformation of the structure, which would produce thermal stress through the spontaneous constraints of the object structure [16]. The determination of the structure temperature field is a prerequisite for obtaining its thermal strain and thermal stress. The temperature value of each point inside the structure is called the temperature field, which is a function of the position coordinates (x, y, z, t) and time t , and it is usually expressed as follows [19]:

$$T = T(x, y, z, t). \quad (1)$$

There are three ways of heat transfer, including heat conduction, thermal convection, and heat radiation, caused by the temperature difference in the nature [20]. The change of the inside heat would result in changes in the object temperature without considering the phase change. When the temperature increment of micro object unit is $\partial T/\partial t$ in unit time, the saving heat dQ could be expressed as follows [19]:

$$dQ = \rho c \frac{\partial T}{\partial t} dx dy dz, \quad (2)$$

where ρ is the material density (kg/m^3) and c is the material specific heat ($\text{J}/(\text{kg}\cdot\text{K})$). In the finite element analysis, the relationship between the temperature change at each node of micro body and the saving heat of the micro volume can be obtained by the temperature field control equation based on energy conservation principle. The differential equation of transient heat conduction inside the orthotropic anisotropic object can be defined as follows [19]:

$$\frac{\partial}{\partial x} \left(k_x \frac{\partial T}{\partial x} \right) + \frac{\partial}{\partial y} \left(k_y \frac{\partial T}{\partial y} \right) + \frac{\partial}{\partial z} \left(k_z \frac{\partial T}{\partial z} \right) + q_b = \rho c \frac{\partial T}{\partial t}, \quad (3)$$

where k_x , k_y , and k_z are the thermal conductivity in three orthogonal directions and q_b is the heat flow intensity of the internal heat source.

The temperature field of the object at the initial time is used as the initial condition of the control equation, which can be expressed as follows [19]:

$$T = f(x, y, z, t_0). \quad (4)$$

Boundary conditions are divided into three categories according to the characteristics of the heat conduction process at the boundary of the object:

- (1) The first type of boundary condition: temperature boundary condition. The temperature of the boundary is defined
- (2) The second type of boundary condition: heat flow intensity boundary condition. The heat flow intensity q at the boundary S_q is defined [19].

$$-k_n \frac{\partial T}{\partial n} = q(x, y, z, t). \quad (5)$$

- (3) The third type of boundary condition: convective boundary condition and radiation boundary condition. The convective boundary condition at the boundary S_c can be defined as follows [19]:

$$k_n \frac{\partial T}{\partial n} = q_c = h(T_c - T_s), \quad (6)$$

where q_c is the heat flowing through the unit area in unit time along the n direction, h is the convective heat transfer coefficient of the surface of the object, T_c is the surface temperature of the object, and T_s is the environment temperature. In addition, the radiation boundary condition at the boundary S_r can be defined as follows [19]:

$$k_n \frac{\partial T}{\partial n} = q_r = \kappa(T_r - T_s), \quad (7)$$

where q_r is the heat flowing through the unit area in unit time along the n direction, κ is the equivalent radiation coefficient, T_r is the temperature of the object surface, and T_s is the environment temperature. The temperature field of the whole solving domain can be uniquely determined by the complete boundary condition based on the control Equation (3).

After the determination of the temperature field, the strain caused by the temperature variation can be obtained according to the relationship between the temperature and the thermal deformation, as well as the additional Hooke's Law [21]. The strain ε can be defined as follows:

$$\{\varepsilon\} = \{\varepsilon_E\} + \{\varepsilon_T\}, \quad (8)$$

where $\{\varepsilon_E\}$ is the elastic strain and $\{\varepsilon_T\}$ is the thermal strain. Based on minimum potential energy principle, the unit stress could be defined as follows:

$$\{\sigma\}^e = [D](\{\varepsilon\}^e - \{\varepsilon_T\}^e), \quad (9)$$

where $[D]$ is the elastic matrix. If the external load exists, such as the gravity and the surface pressure, then the external load should be assigned to the relevant node, according to equivalence principle, to obtain the thermodynamic solution results based on the finite element method.

2.2. Boundary Condition. In the simulation, the boundary condition was set according to the exhaust gas temperature and flow rate of the A498BPG diesel engine obtained through the bench test. Figure 2 shows the diesel test bench of A498BPG, parameters of which are shown in Table 1.

The full-load operating condition of the A498BPG naturally aspirated diesel engine is shown as in Table 2.

Assuming that the intake and exhaust of a diesel engine are ideal gases and meanwhile in equilibrium, the intake



FIGURE 2: Diesel test bench of A498BPG.

TABLE 1: Parameters of A498BPG diesel engine.

Bore × stroke/mm	98 × 110
Cylinder number	4
Stroke number	4
Compression ratio	18.5
Rated power/rotating speed/kW/r/min	36.8/2400
Intake mode	Naturally aspiration
Cooling method	Water cooling
Displacement/L	3.319

TABLE 2: The operation conditions of A498BPG diesel engine at full load and idling speed.

	Revolution speed (r/min)	Torque (nm)	Exhaust temperature (°C)	Exhaust flux (kg/h)
Full load	2400	144.4	544	219
Idling speed	792	0	108	133

and exhaust processes are simple compressible thermodynamic systems with the same thermodynamic parameters. T_0 , ρ_0 , and p_0 represent the temperature, density, and pressure of the inlet gas, respectively. T_1 , ρ_1 , and p_1 represent those of the outlet gas, respectively. m_{out} represents the mass flow rate of exhausted gas in exhaust section. d represents the diameter of exhaust pipe. The equation of state of ideal gas is as follows [22]:

$$\frac{p}{\rho} = R_g T, \quad (10)$$

where R_g is a gas constant, which is 287 J/(kg * K).

The continuity equation is as follows [22]:

$$m_{out} = \rho S u, \quad (11)$$

where S is the section area of exhaust pipe and u is the exhaust flow rate.

Based on Equations (10) and (11), the flow rate of the gas in the engine tail pipe can be calculated by Equation (12).

$$u = \frac{4p_0 T_1 m_{\text{out}}}{p_1 \rho_0 T_0 \pi d^2}. \quad (12)$$

It is known that when the engine works at full load and idling load, the exhaust velocity in the exhaust pipe is 6.7 m/s and 18.3 m/s.

The convective heat transfer coefficient characteristic number equation at the condition of fluid sweeping the isothermal plate is selected to calculate the convection heat transfer coefficient at the sensor head, due to that the sensor is installed in a pipe with big size. The characteristic number equation is shown as follows [19]:

$$\text{Nu}_l = 0.664 \text{Re}_l^{1/2} \text{Pr}^{1/3}, \quad (13)$$

where Re_l is the Reynolds number at characteristic length l , which represents the ratio of inertial force to viscous force. Pr is the Prandtl number, which represents the ability of momentum diffusion and heat diffusion. Nu_l is the Nusselt number at characteristic length l , and the Nusselt number is the same at similar convective heat transfer phenomena. The Nusselt number is expressed as follows [19]:

$$\text{Nu} = \frac{hl}{k}, \quad (14)$$

where k is the thermal conductivity of exhaust gas at qualitative temperature, and then the convective heat transfer coefficient h at the surface of the sensor could be expressed as follows:

$$h = 0.664 \text{Re}^{1/2} \text{Pr}^{1/3} k l^{-1}, \quad (15)$$

where l is the total length of the exhaust pipe near the sensor and $L = 0.5$ m. It is calculated that the convective heat transfer coefficient of the PM sensor probe surface is $47 \text{ W}(\text{m}^2 \cdot \text{K})^{-1}$ at the full load of the engine, and $23 \text{ W}(\text{m}^2 \cdot \text{K})^{-1}$ at the idling speed of the engine, with the flow of the high-temperature exhaust gas in the exhaust pipe.

3. Modeling

First, the three-dimensional diagram of the sensor is drawn by the Pro/E software, and then the diagram is imported into the ANSYS multiphysics. Only half of the sensor is simulated due to the axisymmetric structure of the sensor, and the exhaust pipe is represented by a thin plate. In addition, the density, the heat conductivity coefficient, and ratio heat capacity of each should be defined. Figure 3 shows the simplified PM sensor, which includes five parts made of different materials. Table 3 shows the material attribute of the sensor.

The meshing model consisting of 2814 elements, generated by combining the free meshing and local mesh encryption, is shown in Figure 4.

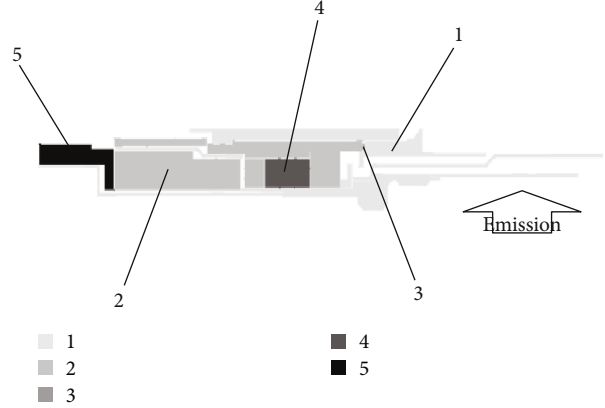


FIGURE 3: Simplified PM sensor in simulation.

4. Results and Discussions

4.1. Reliability Analysis of PM Sensor during the Response Stage of PM Sensor. The operating condition of the sensor, when the engine works at the full load, is really the worst due to the large velocity and the high temperature of the exhaust [23]. Hence, the operating reliability of the sensor at full load can ensure that the sensor could operate normally under any working circumstance. When the engine runs at full load, the exhaust temperature T_s is 544°C , the Reynolds number and the Prandtl number are 7.98×10^5 and 0.65 respectively. Meanwhile, the heat conductivity coefficient k is $0.046 \text{ W}(\text{m} \cdot \text{K})^{-1}$. Then according to Equation (15), the convective heat transfer coefficient of the sensor head marked as h_s is $47 \text{ W}(\text{m}^2 \cdot \text{K})^{-1}$ approximately.

It is necessary that the highest temperature T_d of the sensor base should be lower than 250°C , and the biggest thermal stress marked as δ_{max} , the sensor bears should be lower than allowable stress of the material, where T_d and δ_{max} can be attained through steady-state simulation.

Figure 5 shows the temperature and stress distribution of the sensor when the engine runs at full load, the heat transfer coefficient h_e is $20 \text{ W}(\text{m}^2 \cdot \text{K})^{-1}$, and the environment temperature T_e is 20°C . From Figure 5(a), it shows that the highest temperature of the sensor's head is 520°C , and the air gap in the sensor weakens the heat transfer which causes the fixed base of the sensor being at a lower temperature. The temperature of the front end of the sensor base is up to 227°C , which is lower than the upper working temperature of polytetrafluoroethylene 250°C . Figure 5(b) shows that the highest thermal stress, which is up to 88 MPa, appears at the zone where the section area changes dramatically. And the highest thermal stress 88 MPa is still in the allowable stress range of the material. Thus, it is concluded that the sensor has a high reliability under this severe working conditions, which guarantees the working reliability of the sensor at any operating condition. In addition, the giant temperature difference between the outside and inside of the exhaust pipe causes the high-temperature gradient existing at the thread, which makes a higher thermal stress distribution [24]. By changing the parameter of environment temperature, the temperature

TABLE 3: Material attribute of PM sensor.

	Material	Thermal conductivity ($W(m \cdot k)^{-1}$)	Thermal expansion coefficient (1/K)	Yield strength (MPa)
1	304 stainless steel	16	$1.67E - 05$	205
2	95 porcelain	22.4	$7.50E - 06$	500
3	Copper	398	$1.67E - 05$	290
4	Magnesium oxide & aluminum powder	33	$1.00E - 05$	—
5	Polytetrafluoroethylene	0.244	$1.50E - 05$	24

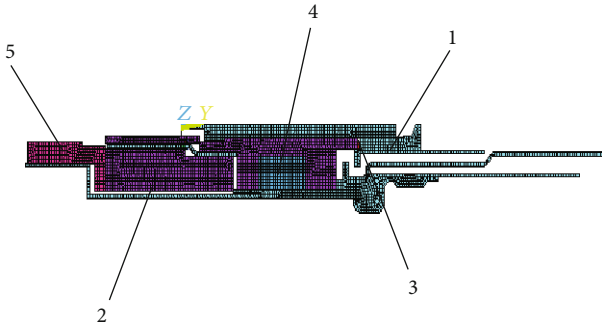


FIGURE 4: Meshing mode of the sensor.

and thermal stress distribution at different environment conditions could be obtained, which is in favor of the sensor reliability research at extreme environment condition.

4.2. The Influence of Outside Environment on the Highest Temperature of the Fixed Base. Figure 6 shows the influence of the outside environment on the highest temperature of the fixed base when the engine is operating at full load. It shows that the highest temperature of the fixed base is positively related to the environment temperature at the same convective heat transfer coefficient, while it is negatively related to the convective heat transfer at the same environment temperature T_e . As a result, any method of reducing the thermal load would be in favor of improving the working condition of the sensor.

The influence of environment parameter h_e on the highest temperature of the fixed base is more obvious than that of the environment parameter T_e because the influence factor dT_d/dh_e is higher than dT_d/dT_e . It is shown that at the same environment temperature, the value of dT_d/dh_e becomes lower with the increment value of h_e . Consequently, the bigger the convective heat transfer coefficient h_e is, the impact it would play on the fixed base is smaller. As a result, the local temperature of the sensor could be effectively reduced through increasing the outside convective heat transfer coefficient within a certain range.

4.3. The Influence of Outside Environment on the Thermal Stress of the Sensor. Figure 7 shows the influence of the outside environment on the biggest thermal stress of the sensor, which is defined as δ_{\max} . It is indicated that the value of δ_{\max} is negatively related to the environment temperature T_e when the outside convective heat transfer coefficient h_e is fixed, while it is positively related to the value of h_e when

the value of T_e is fixed. As a result, any method of reducing the local temperature difference would be in favor of reducing the local thermal stress. The environment parameter h_e has a more obvious effect on the biggest thermal stress than T_e , due to that the value of $d\delta_{\max}/dh_e$ is higher than the value of $d\delta_{\max}/dT_e$. In addition, the value of $d\delta_{\max}/dh_e$ is smaller with the value of h_e increasing at the same environment temperature; thus, the bigger the convective heat transfer coefficient h_e is, the effect it has on the local thermal stress of the sensor is smaller.

Both the increase of the convective heat transfer coefficient and the decrease of environment temperature will increase the local temperature gradient and thermal stress. However, the biggest local thermal stress of the sensor is just up to 115 MPa when the convective heat transfer coefficient reaches to $40 W(m^2 \cdot k)^{-1}$ and environment temperature declines to $0^\circ C$. As a result, the sensor could work reliably under severe working conditions. It is concluded that the increase of convective heat transfer coefficient in a wide range would not only cause the thermal damage of the sensor but also it is in favor of reducing the thermal load of the sensor base.

From Figure 7, it shows that the local thermal stress is the biggest when the convective heat transfer coefficient h_e is $40 W(m^2 \cdot K)^{-1}$, and the environment temperature T_e is $0^\circ C$. Under this circumstance, the point where the biggest thermal stress appears is marked as point A.

Figure 8 shows how the temperature, temperature gradient, and thermal stress vary with time at point A. It is shown that all of them increase sharply at point A before 90 s, and the thermal stress has its biggest value of 128 MPa after 105 s. Then, the temperature increases slowly, and the thermal stress reduces ultimately to 115 MPa with the temperature gradient declining. It is concluded that the thermal stress applied on the sensor is always allowable.

4.4. The Reasonable Heating Power of PM Sensor in the Process of Cold Starting. From the cold starting to the stable idling of the engine, the temperature distribution and stress distribution of the sensor are simulated with the heating power ranging from 10 W to 500 W. The optimum heating power that ensures energy consumption lower and heating efficiency higher could be obtained by comparing the cold starting time and the biggest thermal stress after the cold starting under different heating power values. The obtained optimum heating power simulated at the temperature $0^\circ C$ could guarantee the reliable operation of the sensor at higher

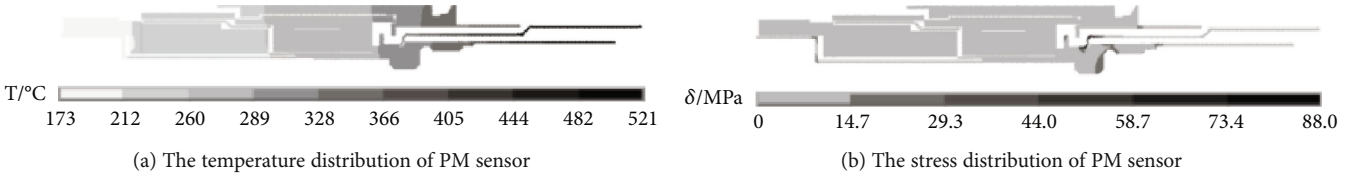


FIGURE 5: The temperature and stress distribution of PM sensor at full load.

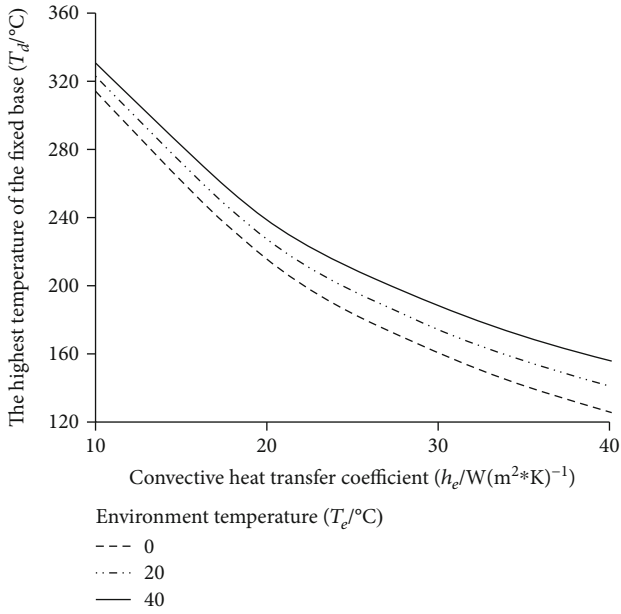


FIGURE 6: Relationship between T_d and external environment under full load condition.

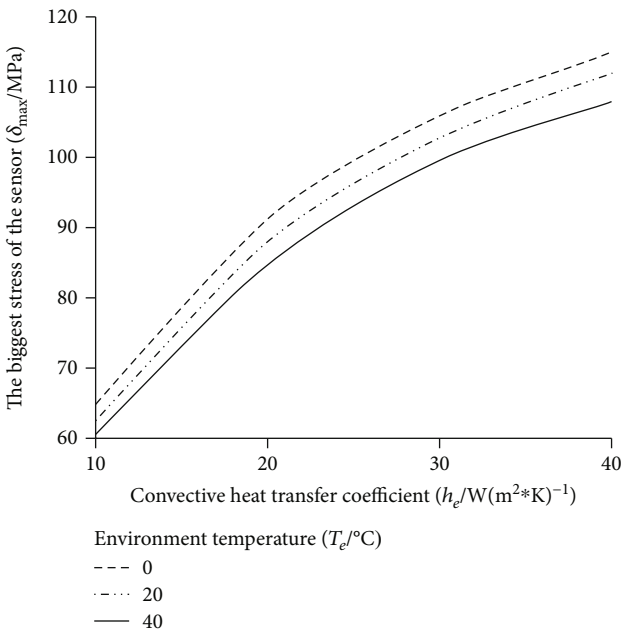


FIGURE 7: Relationship between δ_{max} and external environment under full load condition.

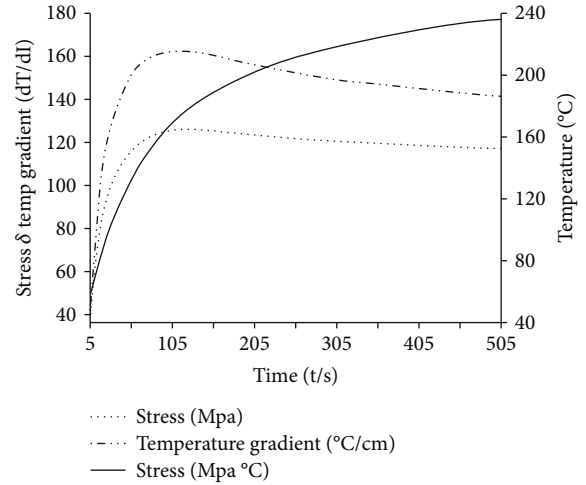


FIGURE 8: Transient condition of max point of thermal stress in the sensor.

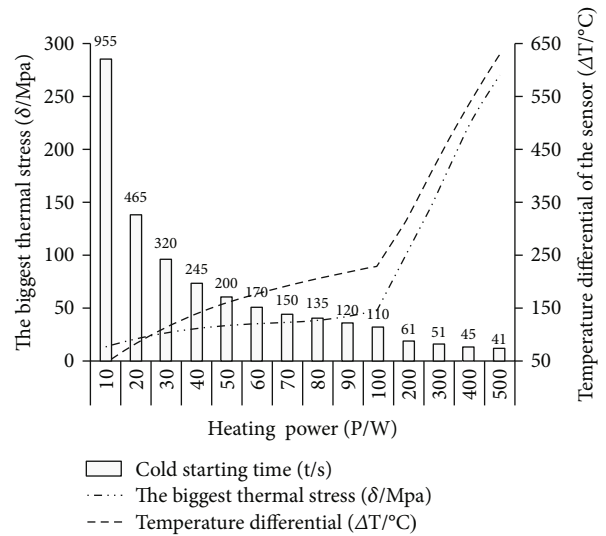


FIGURE 9: Effect of the heating power of sensor at cold start condition.

temperature. Table 2 shows the exhaust environment when the engine works at the idling speed.

Figure 9 shows that the biggest temperature difference is marked as ΔT , and the biggest local thermal stress is marked as δ . It also shows the variation of ΔT , δ , and the cold starting time with the heating power ranging from 10 W to 500 W. It

is indicated that the cold starting time reduces with the increase of the heating power. However, the increase of the heating power would not only result in energy consumption but also lead to the increase of ΔT and δ . In addition, the cold starting time increases sharply with the heating power declining. To determine the reasonable heating power, the variation trend of each parameter should be taken into consideration. The value of dt/dP is approaching to zero with the heating power increasing continuously. As shown in Figure 9, the cold starting time of the sensor is 170 s when the heating power is 60 W, and the cold starting time would not be reduced effectively with the heating power increasing continuously, which would also enlarge the structure thermal stress. It is concluded that the heating power of 60 W could guarantee the cold starting request with the biggest thermal stress being 35.8 megapascals.

5. Conclusions

The transient and steady-state simulation of the temperature and thermal stress are conducted according to the boundary conditions obtained from the engine test bench, and the following conditions were arrived:

- (1) Although the increase of convective heat transfer coefficient leads to the increase of local stress, the overall thermal load of the sensor is reduced. Thus, the sensor can operate reliably over long periods of time at different engine operating environments
- (2) In the transient simulation of the structure stress of the sensor, the external environment resulting in the largest thermal stress is selected as the boundary condition. The result shows that in the cold starting process of the engine, the local thermal stress of the sensor increases first and then decreases, and reaches the peak after about 90 s. The maximum thermal stress of the sensor during cold start is always less than the allowable stress of the material
- (3) In the study of the heating power of the sensor ceramic heating body at the cold start of engine, it turns out that the cold starting time of the sensor decreases exponentially with the increase of the power of the ceramic heating body and the local thermal stress increases linearly. Thus, there is a trade-off between the cold starting time and the local thermal stress when selecting the optimum heating power
- (4) Leakage current PM sensor can operate steadily at various loads, including cold starting and full load. The external environment requirement for sensor working is not strict. It implies that the collection of PM concentration signals can be conducted under the harsh working conditions

A further study will be performed for commercial application in the future. The movement state of particles and the output signal of the sensor under different sensor

structures need to be studied and analyzed to further explore the prototype mechanism of the leakage current PM sensor and the correlation function between sensor signal and structure.

Data Availability

The data used to support the findings of this study are available from the corresponding author upon request.

Conflicts of Interest

The authors declare that they have no financial and personal relationships with other people or organizations that can inappropriately influence their work; there is no professional or other personal interests of any nature or kind in any product, service, and/or company that could be construed as influencing the position presented in, or the review of, the manuscript entitled.

Acknowledgments

The authors acknowledge support from the National Natural Science Fund of China (51876085), the National Engineering Laboratory for Mobile Source Emission Control Technology (NELMS2017C05) in China, the 2016 Priority Research Project (BE2016141) in Jiangsu Province of China, and the Sichuan Key Laboratory for Automotive Measurement Control and Safety (QCKK2019-001) in Sichuan Province of China.

References

- [1] P. Li, P. Tan, D. Lou, and Z. Hu, "Exhaust after-treatment technology for heavy-duty diesel engine meeting the Primary 5 standard," *Vehicle Engine*, vol. 4, pp. 1–5, 2010.
- [2] S. Shuai, T. Tang, Y. Zhao, and L. Hua, "Present situation and forecast of emission regulation and after-treatment technology for diesel vehicle," *Journal of Automotive Safety and Energy*, vol. 3, no. 3, pp. 200–217, 2012.
- [3] Commission Regulation (EU), *TCMV 19 Dec (2012)—technical committee—December 2011, No 459/2012*, 2012.
- [4] N. M. Van and D. Trudell, *Diagnostics for Diesel Particles Filters*, SAE Technical Paper, 2004.
- [5] J. Lavy, C. N. Millet, B. Reveille et al., "PM sensor development for on-board diagnosis of diesel particulate filter failures," in *16th ETH Conference on Combustion Generated Nanoparticles*, Zurich, June 2012.
- [6] O. Brunel, F. Duault, B. Youssef, J. Lavy, and Y. Creff, "Smart soot sensor for particulate filter OBD," in *Advanced Microsystems for Automotive Applications 2013. Lecture Notes in Mobility*, J. Fischer-Wolfarth and G. Meyer, Eds., Springer, Heidelberg, 2013.
- [7] A. Hoepfner, C. A. Roduner, and P. M. Sensor, *Based On-Board Diagnosis of Particulate Filter Efficiency*, SAE 2013 World Congress & Exhibition, 2013.
- [8] D. Grondin, A. Westermann, P. Breuil, J. P. Viricelle, and P. Vernoux, "Influence of key parameters on the response of a resistive soot sensor," *Sensors and Actuators B: Chemical*, vol. 236, pp. 1036–1043, 2016.

- [9] T. T. Diller, M. J. Hall, and R. D. Matthews, *Further development of an electronic particulate matter sensor and its application to diesel engine transients*, SAE Technical Paper Series, 2008.
- [10] S. Amanatidis, L. Ntziachristos, Z. Samaras, K. Janka, and J. Tikkanen, "Applicability of the Pegasor particle sensor to measure particle number, mass and PM emissions," SAE Technical Papers, 2013-24-0167, 2013.
- [11] J. Steppan, B. Henderson, K. Johnson et al., *Comparison of an On-Board, Real-Time Electronic PM Sensor with Laboratory Instruments Using a 2009 Heavy-Duty Diesel Vehicle*, SAE International, 2011.
- [12] M. M. Maricq and D. Bilby, "The impact of voltage and flow on the electrostatic soot sensor and the implications for its use as a diesel particulate filter monitor," *Journal of Aerosol Science*, vol. 124, pp. 41–53, 2018.
- [13] D. Bilby, D. J. Kubinski, and M. M. Maricq, "Current amplification in an electrostatic trap by soot dendrite growth and fragmentation: application to soot sensors," *Journal of Aerosol Science*, vol. 98, pp. 41–58, 2016.
- [14] EmiSense Technologies, LLC, *EmiSense develops next-generation emissions sensors* [EB/OL]<http://emisense.com/>.
- [15] J. Wang, D. Tang, S. Wang, Z. Zhu, N. Li, and L. Chen, "New leakage current particulate matter sensor for on-board diagnostics," *Journal of Sensors*, vol. 2016, Article ID 5380646, 8 pages, 2016.
- [16] M. J. Turner, R. W. Clough, H. C. Martin, and L. C. Topp, "Stiffness and deflection analysis of complex structures," *Journal of the Aeronautical Sciences*, vol. 23, no. 9, pp. 805–823, 1956.
- [17] R. W. Clough, "The finite element method in plane stress analysis," in *Proceedings of 2nd ASCE Conference on Electronic Computation*, Pittsburgh, PA, USA, September 1960.
- [18] Y. Takeuchi, *Thermal Stress*, Science Press, Beijing, 1982.
- [19] J. P. Holman, *Heat Transfer*, McGraw-hill, 1963.
- [20] S. Yang and W. Tao, *Heat Transfer*, Higher Education Press, Beijing, 2006.
- [21] F. Yetai, *Theory and Application of Mechanical Thermal Deformation*, National Defense Industry Press, Beijing, 2009.
- [22] F. M. White, *Fluid Mechanics*, McGraw-hill, 2009.
- [23] L. Zhou, *Internal Combustion Engine*, China Machine Press, Beijing, 2010.
- [24] X. Wu, L. Zhuge, Z. Wu, and C. Ye, *Physical Properties and Detection of Material*, Science Press, Beijing, 2012.



Hindawi

Submit your manuscripts at
www.hindawi.com

